Wang, Dehui; Sun, Qiangqiang; Hokkanen, M.J.; Zhang, Chenglin; Lin, Fan-Yen; Liu, Qiang; Zhu, Shun-Peng; Zhou, Tianfeng; Chang, Qing; He, Bo; Zhou, Quan; Chen, Longquan ; Wang, Zuankai; Ras, Robin; Deng, Xu

Design of robust superhydrophobic surfaces

Published in:
Nature

DOI:
10.1038/s41586-020-2331-8

Published: 04/06/2020

Document Version
Peer reviewed version

Designing Robust Superhydrophobic Surfaces

Dehui Wang[1], Qiangqiang Sun[1], Matti J. Hokkanen[2,3], Chenglin Zhang[1], Fan-Yen Lin[4], Qiang Liu[5], Shun-Peng Zhu[5], Tianfeng Zhou[6], Qing Chang[7], Bo He[7], Quan Zhou[3], Longquan Chen[8], Zuankai Wang[9], Robin H. A. Ras[2,10*] and Xu Deng[1*]

1. Institute of Fundamental and Frontier Sciences, University of Electronic Science and Technology of China, Chengdu, China

2. Department of Applied Physics, Aalto University School of Science, Espoo, Finland

3. Department of Electrical Engineering and Automation, Aalto University School of Electrical Engineering, Espoo, Finland

4. Bruker Nano Surfaces Division, Santa Barbara, USA

5. School of Mechanical and Electrical Engineering, University of Electronic Science and Technology of China, Chengdu, China

6. Key Laboratory of Fundamental Science for Advanced Machining, Beijing Institute of Technology, Beijing, China

7. Hanergy Chengdu R&D Center, Chengdu, China

8. School of Physics, University of Electronic Science and Technology of China, Chengdu, China

9. Department of Mechanical Engineering, City University of Hong Kong, Hong Kong, China

10. Department of Bioproducts and Biosystems, Aalto University School of Chemical Engineering, Espoo, Finland

The ability of superhydrophobic surfaces to stay dry, self-clean and avoid biofouling is attractive for applications in biotechnology, medicine and heat transfer[1-10]. It requires that water droplets placed on superhydrophobic surfaces have large apparent contact angles ($\theta^* > 150°$) and low roll-off angles ($\theta_{\text{roll-off}} < 10°$), realized with surfaces having low-surface-energy chemistry as well as micro- or nanoscale surface roughness that minimizes liquid-solid contact[11-17]. But rough surfaces where liquid contacts only a small

fraction of their overall area experience high local pressures under mechanical load, making them fragile and highly susceptible to abrasion[18]. Additionally, abrasion exposes underlying materials and may change the local surface chemistry from hydrophobic to hydrophilic[19], leading to the pinning of water droplets. The common assumption thus is that mechanical robustness and water repellency are mutually exclusive surface properties, but we show here that this need not be the case: unprecedented performance levels can be realized when structuring surfaces at two different length scales, with a nanostructure design to provide water repellency and a microstructure design to provide durability. The microstructure is an interconnected surface frame with 'pockets' that house highly water repellent and mechanically fragile nanostructures and prevent their removal by abradants greater than the frame size. We apply this armor concept to various substrates such as silicon, ceramic, metal and transparent glass, and show that the obtained superhydrophobic surfaces preserve their water repellency even after sharp steel blade and sandpaper abrasion. We anticipate that the transparent, mechanically robust self-cleaning glass might solve the dust contamination issue that causes efficiency loss in solar cells, and that the armor design strategy can also guide the development of other materials that need to retain effective self-cleaning, anti-fouling or heat transfer abilities in harsh operating environments.

While minimizing liquid-solid contact area is widely used to enhance superhydrophobicity, it results in fragile surface textures and poor wear resistance[20]. Various approaches have been explored to address this problem, e.g.: (i) strengthening the bonding between coating and substrate by using an adhesion layer[21,22], (ii) bearing the abrasion force by randomly introducing discrete microstructures[23-26] and (iii) allowing abrasion by sacrificing the upper layers of a self-similar structure[27-29], but have allowed only modest improvements of robustness (Supplementary Video 1). To resolve this bottleneck, we divide the mechanical durability and non-wettability and implement them at two different length scales: the nanostructures provide excellent water repellency, whereas the microstructures act as armor to resist abrasion (Fig. 1a, Supplementary Fig. 1, Supplementary Video 2 and Supplementary Discussion section 2.1). The first design feature is an interconnected frame that prevents abradants greater than the frame size from removing the nanostructures (Figs. 1b and c). Furthermore, the interconnectivity enhances mechanical robustness as inspired by nature, e.g. springtail skin and honeycomb. Additional design features must be considered to ensure wettability is not compromised. Here, we explore the relation between the liquid-solid contact fraction f, the Young's contact angle θ_Y and the apparent contact angle θ^* using the Cassie-Baxter model:

$$\cos\theta^* = f(1+\cos\theta_Y)-1 \qquad (1)$$

In the Cassie-Baxter wetting state, the role of Young's contact angle is investigated by plotting equation (1) with θ_Y as a parameter in Fig. 1d. The difference ($\Delta\theta^*$) between the θ^* values of the hydrophobic ($\theta_Y = 120°$) surface and hydrophilic ($\theta_Y = 0°$) surface gets smaller as f decreases (Fig. 1d). This indicates that the contribution of the material's surface chemistry (θ_Y) on the liquid repellency (θ^*) diminishes by minimizing f. In other words, even if during abrasion the top surface would be altered from hydrophobic to hydrophilic, the armored surface can still repel water if f is very small.

The mechanical stability of microstructures is dominated by the geometry. To optimize the robustness, we adjust the angle (α) between the sidewall and the substrate of the microstructures (Figs. 1e and f) while maintaining the top contact area constant. From structural mechanics point of view, increasing α is usually an effective way to strengthen the structural stability of architecture, such as in case of the ancient Egyptian pyramid and the gravity dam. To confirm this principle, microstructures with different α were modeled and the stress distributions under fixed load were simulated using multipurpose Finite Element (FE) analysis (Supplementary Fig. 2). The 3rd principal stress ($|\sigma|$) reduces significantly, and thus stability of the microstructures improves vastly, as α increases (Fig. 1f). On the other hand, liquid-solid contact fraction of the microstructures, $f_{\mathrm{orig}}^{\mathrm{micro}}$, will increase to $f_{\mathrm{half}}^{\mathrm{micro}}$ when half of the height is abraded (Figs. 1e and f, Supplementary Fig. 3 and Supplementary Discussion section 2.2). The increase of $\Delta f^{\mathrm{micro}}=f_{\mathrm{half}}^{\mathrm{micro}}-f_{\mathrm{orig}}^{\mathrm{micro}}$ with α means the liquid-solid contact area increases, i.e., the liquid adhesion force increases. As shown in Fig. 1f, an optimum regime ($\alpha \sim 120°$) emerges where both superhydrophobicity and mechanical stability can be balanced and guaranteed. The second and third design features for the armor are thus low f^{micro} and α near 120°.

We constructed the armor surface following these three design features with a framework consisting of microscale inverted pyramidal cavities. Using parameters including the width of the ridge *w*, i.e., the distance between the adjacent holes*,* width of the cavity *l,* and the height *h* (Fig. 2a), the liquid-solid contact fraction (f^{micro}) can be tailored according to equation (2).

$$f^{\mathrm{micro}}=\frac{2wl+w^2}{(w+l)^2} \qquad (2)$$

The inverted pyramidal microstructures with $\alpha \sim 125°$ were be manufactured on silicon substrates by photolithography (Fig. 2b, Supplementary Figs. 4 and 5). For comparison, the pillar and pyramidal microstructures were fabricated on silicon surfaces with the same f^{micro} as the inverted pyramidal microstructures (Supplementary Fig. 6). The mechanical stability of those surface textures was characterized by micro-indentation. As shown in Fig. 2c, the load-displacement curves of those surfaces exhibited some breakpoints. This is due to the saltation of loading and displacement caused by the obvious fracture of the microstructures. The fracture of the microstructure at the first apparent breakpoints (i, ii and iii) in the corresponding curve was shown in Supplementary Fig. 7. The inverted pyramidal structures can resist the highest pressure and have experienced only minor damage. These results agree well with the FE simulation and verify the rationality of principle for the armor design (Fig. 2d and Supplementary Fig. 8). We also fabricated inverted pyramidal structures on ceramic, metal, transparent glass and flexible PDMS substrates by embossing technology (Fig. 2e-g, Supplementary Figs. 9-13). From the engineering perspective, this armor approach can also be applied on curved substrates and is scalable by using roll-to-plate printing technology (Supplementary Figs. 10c and d, Supplementary Video 3).

The armored surface exhibits superhydrophobicity after integrating a nanostructured coating. Here, the fluorinated fractal nanoclusters of silica were used as a model superhydrophobic nanomaterial (Fig. 3a, Supplementary Figs. 14 and 15). After repeated scraping by a steel blade, the armor microstructure shows excellent resistance to the vertical pressure and shear force, and the fractal nanostructure in between the armor keeps itself intact (Fig. 3b). It is notable that the abrasion removes the fluorinated silane layer from the top of armor microstructures altering local wetting from hydrophobic (θ_Y = 115±1°) to hydrophilic (θ_Y = 45±0.5°, Supplementary Table 1). Using laser scanning confocal microscopy, we confirmed that the air-water-solid composite interface at microscale was very stable, since the air-liquid-solid three-phase contact line is supported by nanoscale superhydrophobic materials (Figs. 3a and c). The water repellent nanostructures can prevent the sagging of the liquid/air interface caused by the Laplace pressure and the entire system stayed at the constrained equilibrium Cassie-Baxter state (Figs. 3a and c, Supplementary Fig. 16). To systematically evaluate the impact of abrasion on superhydrophobicity, a series of armored superhydrophobic surfaces with different open width of the cavities (l) and liquid-solid contact fraction (f^{micro}) were prepared, and θ^* and $\theta_{\text{roll-off}}$ on the surfaces before and after abrasion were measured. All experimental data are consistent with the theoretical model equation (3) (Fig. 3d).

$$\cos\theta^* = f^{\text{micro}}\left(\cos\theta_{\text{Y}}^{\text{micro}}+1\right) + f^{\text{nano}}(\cos\theta_{\text{Y}}^{\text{nano}}+1) - 1 \qquad (3)$$

We defined f^{micro} as the liquid-solid contact fraction of armor microstructure and f^{nano} as the liquid-solid contact fraction of nanostructure in the armor (see Fig. 3a and Supplementary Discussion section 2.3). Both the static contact angle and the roll-off angles in Figs. 3d and e show the armored surfaces can keep its super-repellency after abrasion if f^{micro} was lower than 8%. Those results are consistent with the ideal Cassie-Baxter model, also suggesting that non-wettability was independent of the scale of inverted pyramidal structures. However, the smaller the scale of the armor structures, the more extensive the changes to the liquid-solid contact fraction (Δf^{micro}) after the same abrasion fracture (Supplementary Fig. 17). The suitable armor size can be tailored for various practical application situations.

To further understand the effect of the liquid-solid contact fraction for controlling the non-wettability after abrasion, pull-off force maps of the armored superhydrophobic surfaces were measured by scanning droplet adhesion microscopy. The armor microstructured surfaces (f^{micro} ~ 2% and 7.8%) were measured before and after abrasion. As indicated in Extended Data Fig. 1 and Fig. 3f, the pull-off forces with different f^{micro} show a similar result before abrasion. After abrasion, the damage of the hydrophobic layer on the armor top resulted in a rise of pull-off forces at the same f^{micro}. However, the pull-off forces on the high f^{micro} (~ 7.8%) rose more rapidly than on the low f^{micro} (~ 2%) surfaces, which corresponds with the trend of $\theta_{\text{roll-off}}$ (Fig. 3e). Extended Data Fig. 2 illustrates a water jet impinging onto the armored superhydrophobic surface before and after abrasion with an incidence angle of 28° and a volume velocity of 6 ml min^{-1}. It agrees with our previous wettability measurement, with a lower f^{micro} the deflected angles were higher, i.e., less energy dissipation occurred when the water bounced away from the surface. Similar variations by water droplets impacting experiments also supported this principle (Extended Data Fig. 3 and Supplementary Video 4).

To demonstrate that the interconnected frame architecture, i.e., individual cavities designed with a large sidewall angle, is a generic concept to achieve the superior performances, we further fabricated inverted triangular pyramidal (tri-pyramidal) and inverted hexagonal pyramidal (hex-pyramidal) structures on silicon, metal and ceramic substrates (Figs. 3g and h, Supplementary Figs. 18-20), respectively. The FE modeling demonstrated the stress distribution on these interconnected frame architectures is relatively uniform, showing comparable mechanical robustness with the inverted pyramidal armor structure. As shown in Figs. 3i and j, after repeated scraping by a steel blade, the inverted tri-pyramidal and hex-pyramidal interconnected architectures ensure robust superhydrophobic property.

In real-world applications, surfaces are exposed to repeated abrasion and we further examine the long-term mechanical durability of armored superhydrophobic surfaces with different microstructures. The abrasion was conducted by using a polypropylene (PP) probe as the indenter with a defined vertical pressure and reciprocating linear abrasion (see Fig. 4a, Supplementary Fig. 21 and Supplementary Video 5). As shown in Fig. 4b, c, the armored superhydrophobic surfaces maintained the static contact angle above 150° and roll-off angle less than 12° even after 1000 abrasion cycles, and present an ideal resistance to the shear force and protection for the silica nanomaterials inside (Supplementary Figs. 21-22). To illustrate the mechanical durability of our armored superhydrophobic surfaces, we benchmark the critical fracture force, i.e., the maximum force to destroy the superhydrophobicity and the maximum number of abrasion cycles against conventional superhydrophobic surfaces (see Supplementary Fig. 23 and Supplementary Methods section 1.11c). Specifically, the maximum number of abrasion cycles are measured to be more than 1000, which is 10 times higher than for conventional superhydrophobic surfaces (Fig. 4d). The mechanical robustness of the armored surfaces was also demonstrated by tape-peeling tests, ASTM standard Taber abrasion tests and ultra-sharp object scratch tests (Supplementary Figs. 24-26). We have also conducted more severe durability tests, including thermal stability (100 ¡C for 16 days), chemical corrosion (immersion in aqua regia or 2.5 M of NaOH solution for 4 h), high-speed jet impact (water jet at 32.6 m s^{-1}, *We* ~ 36,478, Supplementary Video 6) and the tolerance of condensation-induced failure at high-humidity environments (Supplementary Figs. 27-34). It was found that the armored surfaces maintained their superhydrophobicity even under extremely harsh conditions.

These findings demonstrate the value of the armor concept for improving the mechanical stability of superhydrophobic surfaces. The decoupling strategy at the heart of this design framework allows us to perfectly balance mechanical robustness, non-wettability and optical transparency (Fig 4e, Supplementary Video 7). We use this to create a robust and transparent self-cleaning topcoat for solar cells that maintains their high energy conversion efficiency through passive removal of dust contamination, which could save massive amounts of freshwater, labor and costs associated with the traditional cleaning process (Figs. 4e-f, Extended Data Figs. 5 and 6 and Supplementary Fig. 35)[30]. Beyond this initial proof-of-concept illustration, the generality and effectiveness of our design principle and strategy promises to move superhydrophobic surfaces toward real-world applications.

References

1 Wong, T.-S., Sun, T., Feng, L. & Aizenberg, J. Interfacial materials with special wettability. *MRS Bull.* **38**, 366-371, doi:10.1557/mrs.2013.99 (2013).

2 Liu, M., Wang, S. & Jiang, L. Nature-inspired superwettability systems. *Nat. Rev. Mater.* **2**, 17036, doi:10.1038/natrevmats.2017.36 (2017).

3 Bhushan, B. & Jung, Y. C. Natural and biomimetic artificial surfaces for superhydrophobicity, self-cleaning, low adhesion, and drag reduction. *Prog. Mater. Sci.* **56**, 1-108, doi:10.1016/j.pmatsci.2010.04.003 (2011).

4 Schmidt, D. L., Brady, R. F., Lam, K., Schmidt, D. C. & Chaudhury, M. K. Contact angle hysteresis, adhesion, and marine biofouling. *Langmuir* **20**, 2830-2836, doi:10.1021/la035385o (2004).

5 Jung, S., Tiwari, M. K., Doan, N. V. & Poulikakos, D. Mechanism of supercooled droplet freezing on surfaces. *Nat. Commun.* **3**, 615, doi:10.1038/ncomms1630 (2012).

6 Bahng, J. H. *et al.* Anomalous dispersions of 'hedgehog' particles. *Nature* **517**, 596-599, doi:10.1038/nature14092 (2015).

7 Rastogi, V. *et al.* Synthesis of light-diffracting assemblies from microspheres and nanoparticles in droplets on a superhydrophobic surface. *Adv. Mater.* **20**, 4263-4268, doi:10.1002/adma.200703008 (2008).

8 Lee, S. Y., Rahmawan, Y. & Yang, S. Transparent and superamphiphobic surfaces from mushroom-like micropillar arrays. *ACS Appl. Mater. Interfaces* **7**, 24197-24203, doi:10.1021/acsami.5b07551 (2015).

9 Miljkovic, N. & Wang, E. N. Condensation heat transfer on superhydrophobic surfaces. *MRS Bull.* **38**, 397-406, doi:10.1557/mrs.2013.103 (2013).

10 Pan, S. *et al.* Coatings super-repellent to ultralow surface tension liquids. *Nat. Mater.* **17**, 1040, doi:10.1038/s41563-018-0178-2 (2018).

11 Gao, L. & McCarthy, T. J. The “Lotus Effect” explained: two reasons why two length scales of topography are important. *Langmuir* **22**, 2966-2967, doi:10.1021/la0532149 (2006).

12 Tuteja, A. *et al.* Designing superoleophobic surfaces. *Science* **318**, 1618-1622 (2007).

13 Quéré, D. Wetting and roughness. *Annu. Rev. Mater. Res.* **38**, 71-99, doi:10.1146/annurev.matsci.38.060407.132434 (2008).

14 Butt, H.-J. *et al.* Characterization of super liquid-repellent surfaces. *Curr. Opini. Colloid Interface Sci.* **19**, 343-354, doi:10.1016/j.cocis.2014.04.009 (2014).

15 Liu, T. L. & Kim, C. J. Turning a surface superrepellent even to completely wetting liquids. *Science* **346**, 1096-1100, doi:10.1126/science.1254787 (2014).

16 Sbragaglia, M. *et al.* Spontaneous breakdown of superhydrophobicity. *Phys. Rev. Lett.* **99**, 156001, doi:10.1103/PhysRevLett.99.156001 (2007).
17 Herminghaus, S. Roughness-induced non-wetting. *Europhys. Lett.* **52**, 165 (2000).
18 Tian, X., Verho, T. & Ras, R. H. A. Moving superhydrophobic surfaces toward real-world applications. *Science* **352**, 142 (2016).
19 Milionis, A., Loth, E. & Bayer, I. S. Recent advances in the mechanical durability of superhydrophobic materials. *Adv. Colloid Interface Sci.* **229**, 57-79, doi:10.1016/j.cis.2015.12.007 (2016).
20 Bhushan, B. & Nosonovsky, M. Scale effects in friction using strain gradient plasticity and dislocation-assisted sliding (microslip). *Acta Mater.* **51**, 4331-4345, doi:10.1016/S1359-6454(03)00261-1 (2003).
21 Zhang, W. *et al.* Facile design and fabrication of superwetting surfaces with excellent wear-resistance. *ACS Appl. Mater. Interfaces* **9**, 15776-15784, doi:10.1021/acsami.7b02158 (2017).
22 Lu, Y. *et al.* Robust self-cleaning surfaces that function when exposed to either air or oil. *Science* **347**, 1132-1135, doi:10.1126/science.aaa0946 (2015).
23 Zimmermann, J., Reifler, F. A., Fortunato, G., Gerhardt, L.-C. & Seeger, S. A simple, one-step approach to durable and robust superhydrophobic textiles. *Adv. Funct. Mater.* **18**, 3662-3669, doi:10.1002/adfm.200800755 (2008).
24 Azimi, G., Dhiman, R., Kwon, H. M., Paxson, A. T. & Varanasi, K. K. Hydrophobicity of rare-earth oxide ceramics. *Nat. Mater.* **12**, 315-320, doi:10.1038/nmat3545 (2013).
25 Kondrashov, V. & Ruhe, J. Microcones and nanograss: toward mechanically robust superhydrophobic surfaces. *Langmuir* **30**, 4342-4350, doi:10.1021/la500395e (2014).
26 Zhang, Y., Ge, D. & Yang, S. Spray-coating of superhydrophobic aluminum alloys with enhanced mechanical robustness. *J. Colloid Interface Sci.* **423**, 101-107, doi:10.1016/j.jcis.2014.02.024 (2014).
27 Peng, C., Chen, Z. & Tiwari, M. K. All-organic superhydrophobic coatings with mechanochemical robustness and liquid impalement resistance. *Nat. Mater.* **17**, 355-360, doi:10.1038/s41563-018-0044-2 (2018).
28 Jin, H., Tian, X., Ikkala, O. & Ras, R. H. A. Preservation of superhydrophobic and superoleophobic properties upon wear damage. *ACS Appl. Mater. Interfaces* **5**, 485-488, doi:10.1021/am302541f (2013).
29 Deng, X., Mammen, L., Butt, H.-J., Vollmer, D. Candle soot as a template for a transparent robust superamphiphobic coating. *Science* **335**, 67-70, doi:10.1126/science. (2012).
30 Bergin, M. H., Ghoroi, C., Dixit, D., Schauer, J. J. & Shindell, D. T. Large reductions in solar energy production due to dust and particulate air pollution. *Environ. Sci. Technol. Lett.* **4**, 339-344, doi:10.1021/acs.estlett.7b00197 (2017).

Figure legends

Fig. 1 | Designing the armor. **a**, Cartoons showing the armor strategy to enhance the mechanical stability of the superhydrophobic surface. **b**, **c**, Cartoons showing abrasion damage mechanism on discrete and interconnected microstructures. **b**, In case of discrete microstructures, the abrasion object can be easily inserted in between the microstructures and damage the nanostructure and the microstructure. **c**, Protection in topology by interconnected microstructures. The abrasion object with a size larger than the frame is blocked by the microstructure. **d**, Relation between apparent contact angle θ^* and liquid-solid contact fraction f for ideal Cassie-Baxter state with Young's contact angle θ_Y as a parameter. $\theta_Y = 120°$ is considered as a hydrophobic surface before abrasion, $\theta_Y = 0°$ is considered as the hydrophilic surface after abrasion, and the $\Delta\theta^*$ is the change of the apparent contact angle before and after abrasion. **e**, Cross-section illustration shows the change of contact area on the top of the framework structures when abrasion fractures the height h in half (see Supplementary Fig. 3 and Supplementary Discussion section 2.2 for details). **f**, Influence of mechanical stability and change of the liquid-solid contact fraction Δf^{micro} as function of the sidewall angle (α) (see Supplementary Fig. 3 and Discussion section 2.2 for details).

Fig. 2 | Mechanical stability of the armor structure. **a**, Array of microscale inverted pyramidal cavities as the designed armor. w is the distance between adjacent holes, l is width of the cavities, and h is the height. **b**, Scanning electron micrographs of the inverted pyramidal armor on silicon substrates. **c**, Mechanical characterization of the different structures on silicon substrates by micro-indentation. **d**, Simulated stress distribution on the designed armor model (inverted pyramidal structures). **e-g**, Photographs of the armor structure on ceramic (**e**), metal (**f**) and glass (**g**) substrates (insets show the corresponding scanning electron micrographs, all the scale bars are 50 μm).

Fig. 3 | Evaluation of water repellency after abrasion. **a**, Cartoons showing the water repellency mechanism for the armored nanostructured superhydrophobic surface before and after abrasion. **b**, Scanning electron micrographs with different magnification of silica fractal nanostructures in silicon armor after abrasion. **c**, Confocal microscopy image of a water drop on an armored superhydrophobic surface after abrasion. **d**, The experimental θ^* before (square scatter) and after (hexagonal scatter) abrasion on armored surfaces compared with the theoretical model equation (3). **e**, Comparison of the $\theta_{roll\text{-}off}$ before (red scatter) and after (blue scatter) abrasion. **f**, The pull-off force maps exhibit the water drop adhesion of armored ($w+l$ = 60 μm) superhydrophobic surfaces with different f^{micro} before and after abrasion. **g**, **h**, Scanning electron micrographs show the inverted tri-pyramidal structures on silicon substrate (**g**) and inverted hex-pyramidal structures on anodised aluminium alloy substrate (**h**). **i**, **j**, Apparent contact angle (blue bars) and roll-off angle (red bars) of the silicon inverted tri-pyramidal (**i**) and anodised aluminium inverted hex-pyramidal (**j**) armored surfaces before abrasion (Ba) and after abrasion (Aa). All abrasion was detailed in Supplementary Discussion section 2.3. All error bars indicate standard deviations from at least five independent measurements.

Fig. 4 | Mechanical stability of the armored superhydrophobic surface. **a**, Photograph showing the linear abrasion setup. Normal load ~ 12 MPa. **b**, **c**, The influence of linear abrasion cycles under same load on the water repellency on various superhydrophobic coatings. Error bars indicate standard deviations from at least five independent measurements. **d**, Comparison of the mechanical stability among different superhydrophobic surfaces. The same color area indicates the superhydrophobic surfaces with mechanical stability on the same order of magnitude (see Extended Data Fig. 4 for details). Error bars indicate standard deviations from at least five independent measurements. **e,** Transmission spectra of armored glass (blue line) fabricated using a flat glass substrate (red line). The inset photographs show the transparency and the superhydrophobicity of the armored glass substrate (left inset) and the assembled solar cell using armored glass superhydrophobic surface as the cover plate (right inset). **f**, The energy conversion efficiency of the robust self-cleaning solar panel. (armored glass cover $^{(1)}$ is the solar cell covered with armored glass contaminated by the dust, armored glass cover $^{(2)}$ is the contaminated solar cell after the self-cleaning process) (see Supplementary Fig. 35 for details).

Data availability

The data that support the findings of this study are available from the corresponding author upon reasonable request.

Acknowledgments We thank B.J. Yu, J.L. Yang, Y. Li. and G.W. Zhou for discussions. We thank J.L. Song for providing the samples of the conventional superhydrophobic surfaces. This work was supported by the National Natural Science Foundation of China (21603026), the European Research Council ERC-2016-CoG (725513-SuperRepel), the Academy of Finland (Centres of Excellence Programme 2014–2019), Aalto University AScI/ELEC Thematic Research Programme, Business Finland Project TUTL-SDAM (6798/31/2017).

Author contributions D.W. and X.D. conceived the research and designed the experiments. X.D. and R.H.A.R supervised the research. D.W., Q.S., M.H., C.Z., F.L., T.Z. and Q.C. carried out the experiments. Q.L., S.Z., Z.W., L.C., Q.Z., B. H. built the analytical models. All authors analyzed and interpreted the data and wrote the paper.

Additional information

Supplementary information is available for this paper at https://

Correspondence and requests for materials should be addressed to X.D. (dengxu@uestc.edu.cn) or R.H.A.R. (robin.ras@aalto.fi)

Peer review information

Reprints and permissions information

Extended Data figure legends

Extended Data Fig. 1 | Scanning droplet adhesion microscopy (SDAM) measurement. **a**, Example of droplet adhesion force curve recorded during SDAM sampling of the armored superhydrophobic surface. (I) Prior to making contact with the surface, the droplet is freely suspended from the disc. (II) Once contact is established, the force begins to increase steeply, signifying that the droplet is being pushed against the surface. (III) Following the peak force, the stage is retracted; the force becomes negative as liquid meniscus is elongated. (IV) Ultimately, the droplet detaches from the test surface, which induces a brief period of oscillations. (V) The pull-off force is defined as the difference between the baseline force following detachment, and the global minimum of the curve. **b**, The curves show the pull-off forces of the water drops' adhesion on armored superhydrophobic surfaces, before and after abrasion, as a function of f^{micro}. Pull-off forces were recorded from an area of 2.0 mm $*$ 2.0 mm with 500 μm spacing between each measurement point. Error bars indicate standard deviations from 25 independent measurements.

Extended Data Fig. 2 | Liquid jets impact. **a**, Water jet deflection on the armored superhydrophobic surface before and after abrasion. **b**, The graph shows the change of angles when the water jets (flow rate ~ 6 ml min^{-1}) deflected by the armored superhydrophobic surfaces before and after abrasion. $\Delta\alpha = \alpha_{\mathrm{incident}}-\alpha_{\mathrm{deflected}}$, the $\Delta\alpha$ is plotted as a function of f^{micro}. Inverted pyramidal structures (w+l = 60 μm) on silicon substrates were used for this test. All error bars indicate standard deviations from at least five independent measurements.

Extended Data Fig. 3 | Droplet impact. The graph shows the energy dissipation of the water drops (5.5 µl, 14.0 mm of height) after impact on the armored superhydrophobic surfaces before and after abrasion. The dissipation of energy is plotted as a function of f^{micro}. Inverted pyramidal structures (w+l = 60 µm) on silicon substrates were used for the above test. All error bars indicate standard deviations from at least five independent measurements.

Extended Data Fig. 4 | Comparison of mechanical stability on various superhydrophobic surfaces. The same color area indicates superhydrophobic surfaces with mechanical stability of the same order of magnitude. The x-axis represents the resistance to linear abrasion by PP with a normal load (3 N), the y-axis represents the resistance to scratching by an alloy tip with specified normal load. Each data point represents the capacity of the corresponding surface maintaining its superhydrophobicity under above applied conditions. All samples, including the ones received from collaborators, were abraded in the same setup under similar conditions. Error bars indicate standard deviations from at least nine independent measurements.

Extended Data Fig. 5 | Self-cleaning by the condensate drops. The optical image sequences show the self-cleaning process on armored superhydrophobic surface under fog condition. The red arrows indicate the dust particles (collected from air in Chengdu, China) on the surface. The yellow circle suggests the droplet grabs the dust particle and rolls off. The images were recorded with a Photron SA5 high-speed camera fitted with a macro lens at a frame rate of 5,000 fps. The armored surface placed on an aluminium alloy cold plate with a tilt angle of ～ 45°. The cold plate was controlled at ～ 2 ¡C and the fog ambient with the high relative humidity ～ 95%. The fog consisted of a cloud of air suspended water droplets of an average radius of 3.5 µm, generated using an ultrasonic humidifier.

Extended Data Fig. 6 | Dust removal by the self-cleaning. a, Illustration showing the setup of self-cleaning under fog condensation**. b, c,** Photograph sequences show the fog condensation on dust-polluted planar silicon wafer (**b**) and the dust-polluted armored superhydrophobic surface (**c**). The dust was collected from air in Chengdu, China.

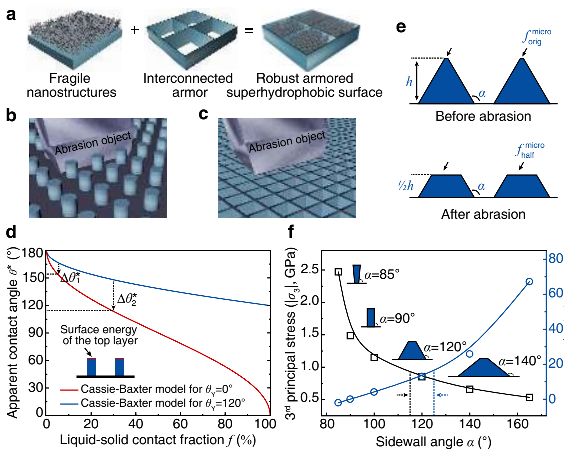

a
Fragile nanostructures
+
Interconnected armor
=
Robust armored superhydrophobic surface
b
Abrasion object
c
Abrasion object
e
h
α
Before abrasion
½h
After abrasion
d
Apparent contact angle θ* (°)
Liquid-solid contact fraction f (%)
Surface energy of the top layer
Cassie-Baxter model for θ_Y=0°
Cassie-Baxter model for θ_Y=120°
f
3rd principal stress (|σ3|, GPa)
Sidewall angle α (°)
α=85°
α=90°
α=120°
α=140°

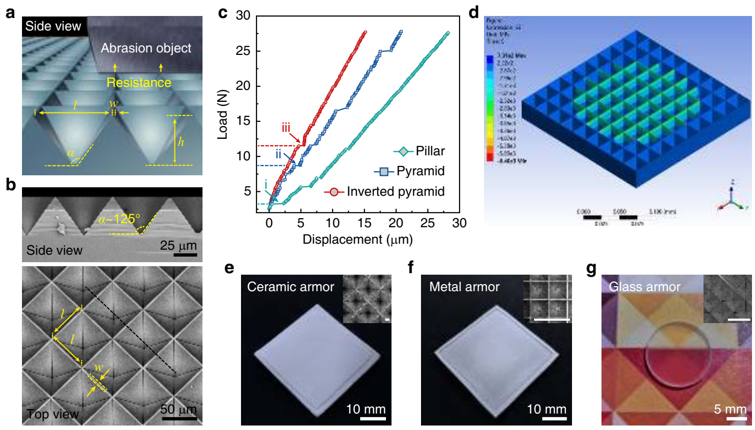
a
Side view
Abrasion object
Resistance
b
α~125°
Side view
25 μm
Top view
50 μm
c
Load (N)
Displacement (μm)
Pillar
Pyramid
Inverted pyramid
i
ii
iii
d
e
Ceramic armor
10 mm
f
Metal armor
10 mm
g
Glass armor
5 mm

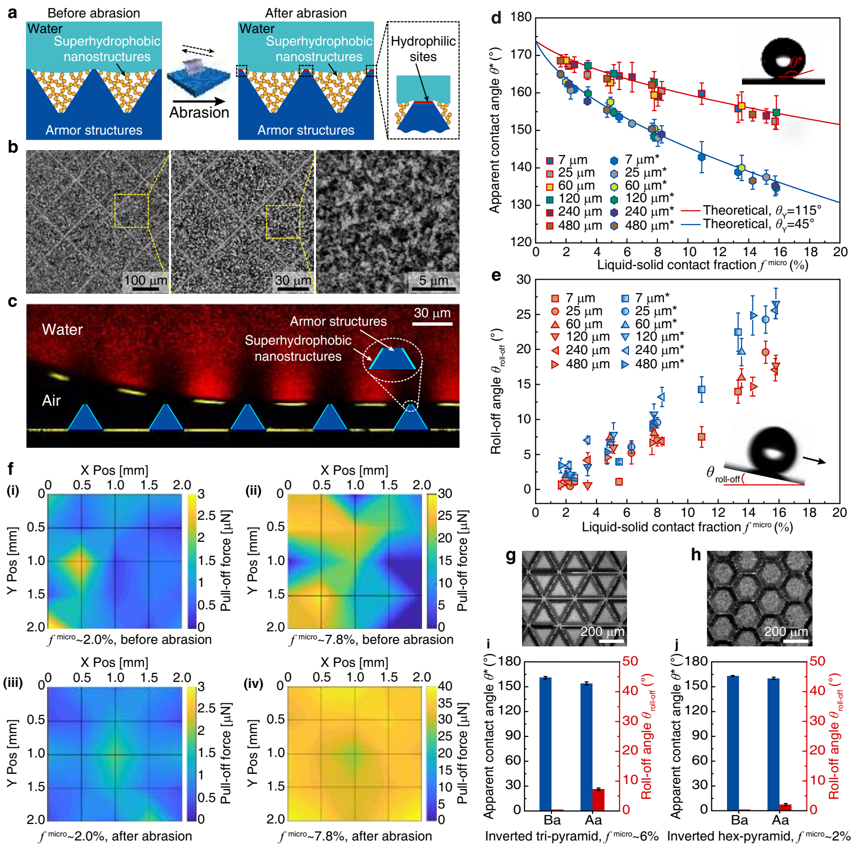

a
Before abrasion
Water
Superhydrophobic nanostructures
Armor structures
Abrasion
After abrasion
Water
Superhydrophobic nanostructures
Armor structures
Hydrophilic sites
b
100 μm
30 μm
5 μm
c
Water
Air
Armor structures
Superhydrophobic nanostructures
30 μm
d
Apparent contact angle θ* (°)
Liquid-solid contact fraction f micro (%)
7 μm
25 μm
60 μm
120 μm
240 μm
480 μm
7 μm*
25 μm*
60 μm*
120 μm*
240 μm*
480 μm*
Theoretical, θY=115°
Theoretical, θY=45°
e
Roll-off angle θroll-off (°)
Liquid-solid contact fraction f micro (%)
7 μm
25 μm
60 μm
120 μm
240 μm
480 μm
7 μm*
25 μm*
60 μm*
120 μm*
240 μm*
480 μm*
θroll-off
f
(i)
X Pos [mm]
Y Pos [mm]
Pull-off force [μN]
f micro~2.0%, before abrasion
(ii)
X Pos [mm]
Y Pos [mm]
Pull-off force [μN]
f micro~7.8%, before abrasion
(iii)
X Pos [mm]
Y Pos [mm]
Pull-off force [μN]
f micro~2.0%, after abrasion
(iv)
X Pos [mm]
Y Pos [mm]
Pull-off force [μN]
f micro~7.8%, after abrasion
g
200 μm
h
200 μm
i
Apparent contact angle θ* (°)
Roll-off angle θroll-off (°)
Ba
Aa
Inverted tri-pyramid, f micro~6%
j
Apparent contact angle θ* (°)
Roll-off angle θroll-off (°)
Ba
Aa
Inverted hex-pyramid, f micro~2%

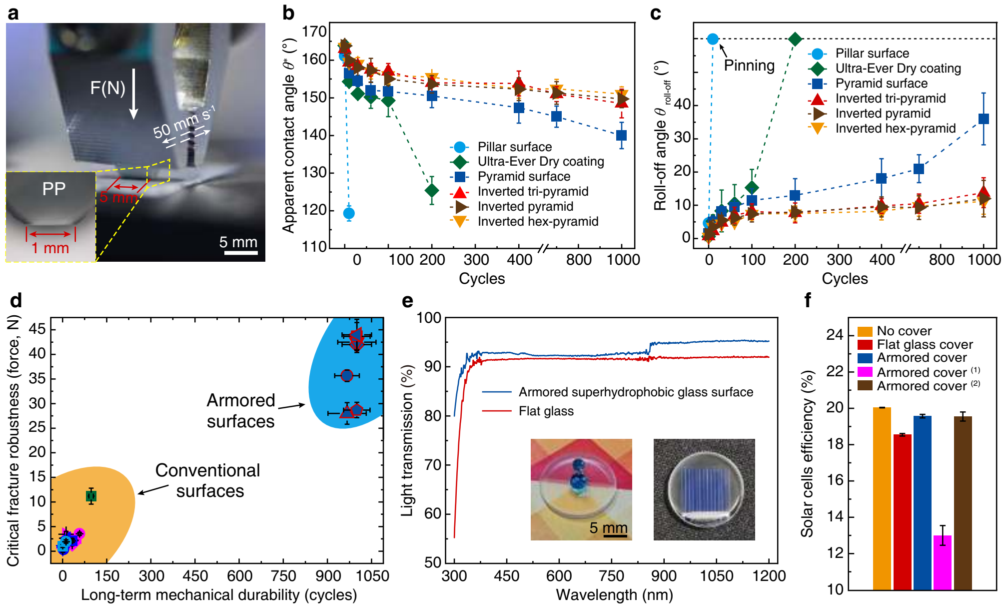

a
F(N)
50 mm s⁻¹
PP
5 mm
1 mm
5 mm
b
Apparent contact angle θ* (°)
Cycles
Pillar surface
Ultra-Ever Dry coating
Pyramid surface
Inverted tri-pyramid
Inverted pyramid
Inverted hex-pyramid
c
Roll-off angle θ roll-off (°)
Pinning
Cycles
Pillar surface
Ultra-Ever Dry coating
Pyramid surface
Inverted tri-pyramid
Inverted pyramid
Inverted hex-pyramid
d
Critical fracture robustness (force, N)
Long-term mechanical durability (cycles)
Armored surfaces
Conventional surfaces
e
Light transmission (%)
Wavelength (nm)
Armored superhydrophobic glass surface
Flat glass
5 mm
f
Solar cells efficiency (%)
No cover
Flat glass cover
Armored cover
Armored cover (1)
Armored cover (2)